ELSEVIER

Nuclear Instruments and Methods in Physics Research B 171 (2000) 204–218

NIM B
Beam Interactions with Materials & Atoms

www.elsevier.nl/locate/nimb

Mechanisms of electronic excitations by low-energy positrons: From finite to extended electronic systems

J. Berakdar *

Max-Planck-Institut für Mikrostrukturphysik, Weinberg 2, 06120 Halle, Germany

Received 4 January 2000; received in revised form 30 March 2000

Abstract

This work deals with the mechanisms of electronic transitions induced by low-energy positrons. For isolated atomic systems we discuss the role of successive binary collisions, the so-called Thomas mechanisms, between the positron, the excited electron and the atomic core. Furthermore, we consider transfer processes in which one of the charged particles is trapped in a low-lying continuum state of one of the reaction participants. In the second part of the paper, we investigate the various pathways for the secondary-electron emission from metallic surfaces following the bombardment by low-energy positrons. From a formal analysis it is shown that the probability rate for the production of an electron–positron pair is connected to the interacting electron–positron two-particle Green operator. The scattering of the interacting positron–electron subsystem from the crystal potential is treated and it is pointed out that a diffraction of the electron–positron pair as a whole might take place leading to characteristic diffraction pattern. The analysis is substantiated by numerical studies for the secondary electron emission from Cu(0 0 1) and Fe(1 1 0) (BCC) samples.

PACS: 34.80G; 3490; 79.20.Kz; 75.30.Ds; 72.10.-d
Keywords: Positron physics; Scattering processes; Ionization processes; Metallic surfaces; Many-body theory; Green function theory; Many-particle spectroscopy

1. Introduction

The utilization of low-energy positron beams for the study of electronic transitions is a routine procedure in fundamental research as well as in material science. For example, the positron-impact ionization of isolated atomic systems leads to a final continuum state consisting of a positron and an electron moving in the field of the residual ion. The spectra of the positron and the electron can be employed as a probe for the dynamics of this correlated few-body scattering state. Generally, the motion of few charged particles above the total fragmentation threshold depends on the charges, masses, energies and momenta of the interacting particles. The mass dependence can be probed, e.g., by contrasting the ionization cross-sections

* Tel.: +49-345-5582666; fax: +49-345-5533221.
E-mail address: jber@mpi-halle.de (J. Berakdar).

0168-583X/00/$ - see front matter
PII: S0168-583X(00)00192-0

for the impact of an equivelocity proton and positron beam. In addition, for a definite amount of energies and momenta of the interacting continuum particles, the open reaction channels as well as the total potential surface can be varied using particle and anti-particle projectiles. This is clearly seen by comparing the electron-impact ionization cross-sections with those due to positron impact. For example, contrasting the final channel achieved upon positron impact with that resulting from electron-impact ionization (two electron in the double continuum of a residual ion), two distinctive differences can be noted:

1. The total potential surface is markedly different in both cases [1]. This results in completely different dynamics, in particular when all particles are close to each other.
2. The indistinguishability of the two electrons leads to characteristic exchange effects in case of an electron beam (the cross-sections are statistical mixtures of triplet and singlet scattering cross-sections). While this effect is absent when using positrons, an additional channel opens, namely that of positronium formation.

On the other hand, classical binary scattering processes are mainly dependent on the masses and momenta of the colliding particles, i.e., whenever quantal effects (including exchange in case of electron beams) are sufficiently small with respect to those arising from classical binary encounters we can expect similar results when using electron or positron beams. This is usually the case for high energies and large separation of the collision products. The importance of the multi-step binary encounters in the positronium formation channel, in particular, and for collision processes in general is well documented [2–10]. In this work we carry out a systematic study of the role of sequential binary collisions in the positron-induced ionization of atomic systems.

It is well established that the cross-section for heavy-particle impact ionization of atoms shows dramatic changes when the ionized electron is ejected into a low-lying continuum state of the scattered projectile [11–22]. For positron impact such effects are also anticipated [10,23–30] to show up in the secondary electron spectrum and have been confirmed by a recent experimental and theoretical study [31,32]. We point out in this work that in fact whenever one particle approaches one of the reaction partners the cross-section decreases or enhances according to the available density of states.

These various aspects of the ionization of atomic systems will be quantified and illustrated by numerical studies in Section 2.

In Section 3, we envisage the secondary electron emission from metallic surfaces upon the disturbance by an incoming low-energy positron beam. Low-energy positrons have long been employed for the investigation of the electronic and crystal structure of solids and surfaces as well as for the investigations of dislocations and crystal lattice defects [34–48]. As stated above, positron beams have an advantage against electrons in that exchange effects are absent. In addition, due to their positive charge positrons feel a repulsive crystal potential, in contrast to electrons. This results in a refractive index less than unity for positrons incident in a glancing mode onto ordered surfaces. This makes positron beams predestinate for the investigation of adsorbates and surface effects. The positronium formation channel can also be utilized for the investigation of material properties by analyzing the angular correlation of the radiation following the annihilation of the positronium and/or the modification of the annihilation parameters due to trapping in crystal lattice defects. In this work, we concentrate on a situation in which a monoenergetic positron beam impinging onto a metallic surface produces secondary electrons. After the excitation process the positron and the vacuum electron are detected in coincidence and their energies and emission directions are determined. The theoretical formulation of this problem is given here for the first time. It is shown that the production of an electron–positron pair is dependent on the interacting electron–positron two-particle Green operator. In reflection-mode emission, the scattering of the interacting positron–electron subsystem from the crystal potential is indispensable. Therefore, we present here a simple treatment in which the crystal potential is approximated by a muffin-tin potential and evaluate the scattering amplitude of the electron–

positron system from this potential. It is found that a diffraction of the electron–positron pair might take place resulting thus in characteristic diffraction pattern in the observed spectrum. The analysis is complemented by numerical studies using Cu(0 0 1) and Fe(1 1 0) (BCC) target samples. Unless otherwise stated, atomic units (a.u.) are used throughout.

2. Mechanisms for the ionization of atomic systems by positrons

In this section, we investigate the pathways for the ionization of an isolated atom in a state $|\varphi_a\rangle$ (with energy ϵ_a) by an incident positron beam with a momentum $\boldsymbol{k}_0$. The vector momenta of the positron and the electron in the final state, $\boldsymbol{k}_{e^+}$ and $\boldsymbol{k}_{e^-}$, respectively, are assumed to be determined simultaneously by the experiment while the residual ion is described by the state vector $|\varphi_c\rangle$ (with an eigenenergy ϵ_c). Thus, the total Hamiltonians in the initial and the final channels can be written as $H_i = h_a + V_i$ and $H_f = h_c + V_f$, respectively. Here h_a and h_c are the Hamiltonians of the undisturbed atom in the initial state and that of the residual ion, i.e., $h_a|\varphi_a\rangle = \epsilon_a|\varphi_a\rangle$ and $h_c|\varphi_c\rangle = \epsilon_c|\varphi_c\rangle$. The potential operator V_f is given by $V_f = H_f - h_c = V_{e^+e^-} + V_{e^+c} + V_{e^-c}$. Here $V_{e^+e^-}$, V_{e^+c} and V_{e^-c} are the two body Coulomb interactions between the positron and the *active* electron, the positron and the final-state ion, and the ionized electron and the ion, respectively. Analogously, the initial state potential V_i has the form $V_i = H_i - h_a = V_{e^+e^-} + V_{e^+c}$. The cross-section $\sigma(\boldsymbol{k}_{e^+}, \boldsymbol{k}_{e^-}, \varphi_c; \boldsymbol{k}_0, \varphi_a)$ for the escaping positron and electron to be detected at the same time with momenta $\boldsymbol{k}_{e^+}, \boldsymbol{k}_{e^-}$ and for the target to go over from the atomic state φ_a into the ionic state φ_c is given by

$$\sigma(\boldsymbol{k}_{e^+}, \boldsymbol{k}_{e^-}, \varphi_c; \boldsymbol{k}_0, \varphi_a) = c|\langle \Psi^- | \Psi^+ \rangle|^2, \tag{1}$$

where $c = (2\pi)^4 k_{e^+} k_{e^-}/k_0$ and

$$|\Psi^-\rangle = \Omega_f^- |\boldsymbol{k}_{e^+}, \boldsymbol{k}_{e^-}, \varphi_c\rangle, \tag{2}$$

$$|\Psi^+\rangle = \Omega_i^+ |\boldsymbol{k}_0, \varphi_a\rangle. \tag{3}$$

The wave operators Ω_f^-, Ω_i^+ are given by

$$\Omega_f^- = \mathbf{1} + G_f^- V_f, \tag{4}$$

$$\Omega_i^+ = \mathbf{1} + G_i^+ V_i, \tag{5}$$

where the many-body Green operators G_f^- and G_i^+ are respectively the resolvent of H_f and H_i, with appropriate boundary conditions. They can be written in the form

$$G_f^- = G_c^- + G_c^- V_f G_f^-, \tag{6}$$

$$G_i^+ = G_a^+ + G_a^+ V_i G_i^+. \tag{7}$$

The Green operators of the atom and the residual ions are denoted by G_a^+ and G_c^-, respectively. From Eqs. (1)–(3), we can write $\sigma = c|\langle \boldsymbol{k}_{e^+}, \boldsymbol{k}_{e^-}, \varphi_c | \Omega_f^{-\dagger} \Omega_i^+ | \boldsymbol{k}_0, \varphi_a \rangle|^2$. Therefore, all dynamical quantities are contained in the product of the two wave operators (this product is usually called the scattering 'S' operator).

$$\begin{aligned} \Omega_f^{-\dagger} \Omega_i^+ &= \left(\mathbf{1} + V_f G_f^+\right)\left(\mathbf{1} + G_i^+ V_i\right) \\ &= \mathbf{1} + G_i^+ V_i + V_f G_f^+ + V_f G_f^+ G_i^+ V_i \qquad (8) \\ &= \mathbf{1} + A + B + C, \qquad (9) \end{aligned}$$

where

$$\begin{aligned} A = {} & G_a^+ V_{e^+e^-} + G_a^+ V_{e^+c} + G_a^+ V_{e^+e^-} G_a^+ V_{e^+e^-} \\ & + G_a^+ V_{e^+c} G_a^+ V_{e^+c} + \cdots, \end{aligned} \tag{10}$$

$$\begin{aligned} B = {} & V_{e^+e^-} G_c^+ + V_{e^+c} G_c^+ + V_{e^-c} G_c^+ \\ & + V_{e^+e^-} G_c^+ V_{e^+e^-} G_c^+ + V_{e^+c} G_c^+ V_{e^+c} G_c^+ \\ & + V_{e^-c} G_c^+ V_{e^-c} G_c^+ + \cdots, \end{aligned} \tag{11}$$

$$\begin{aligned} C = {} & V_{e^+e^-} G_c^+ G_a^+ V_{e^+e^-} + V_{e^+e^-} G_c^+ G_a^+ V_{e^+c} \\ & + V_{e^+c} G_c^+ G_a^+ V_{e^+e^-} + V_{e^+c} G_c^+ G_a^+ V_{e^+c} \\ & + V_{e^-c} G_c^+ G_a^+ V_{e^+e^-} + V_{e^-c} G_c^+ G_a^+ V_{e^+c} + \cdots. \end{aligned} \tag{12}$$

In deriving these relations we made use of the Lippmann–Schwinger equations (6) and (7). The multiple scattering expansions (10)–(12) offer a direct insight into the ionization paths as visualized in Fig. 1(a)–(e): the unity operator in Eq. (9) corresponds to the non-scattered part, the first term in Eq. (10) is an isolated electron–positron

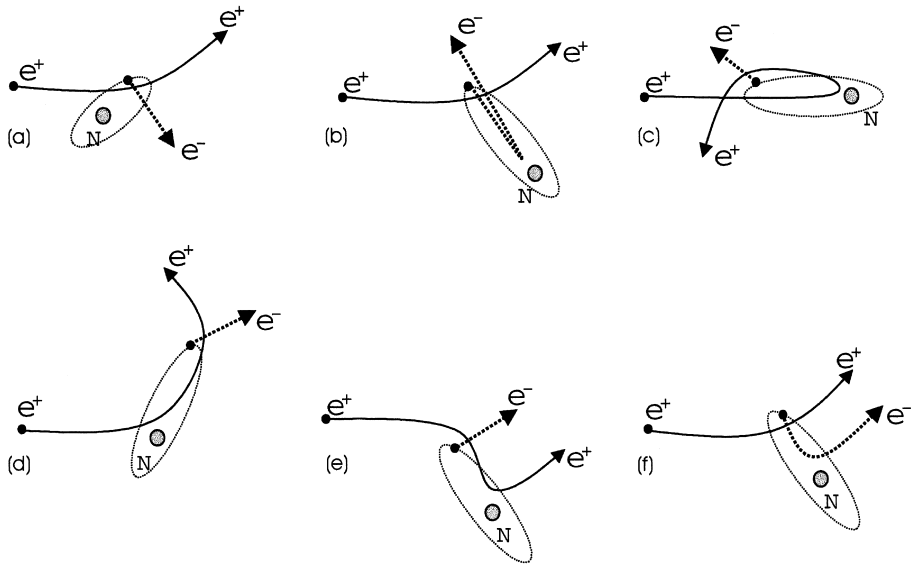

Fig. 1. A schematic drawing of the multi-step scattering processes that correspond to some of the terms in the expansion (10)–(12) (see text for details).

encounter in the field of the atom (Fig. 1(a)), the second term in Eq. (10) can be interpreted as a direct scattering of the positron from the core of the atom (the atom except for the active electron). This contribution is usually neglected due to orthogonality arguments. The rest of Eq. (10) is just higher-order multiple scattering with an interpretation as for the first and the second term being viable. The terms in Eqs. (11) and (12) admit similar interpretation. For example, the second term in Eq. (12) is schematically shown in Fig. 1(c): the positron recoils off the core and subsequently collides with the active electron. Fig. 1(b) corresponds to the fifth term in Eq. (12): after a direct encounter with the positron, the electron scatters from the core of the atom. Figs. 1(e) and (f) correspond to two different terms in the expansion (12) (the third and the fifth term, respectively). Nonetheless, when the electron and the positron emerge after the collision with equal velocities, an experimental set-up cannot distinguish between the contributions of the processes illustrated in Figs. 1(e) and (f). Therefore, interference effects can be expected in this situation. In fact this phenomenon has been first predicted in the positronium formation channel [4].

From Eqs. (10)–(12) it is clear that the development of a single theoretical model that encompasses accurately all the terms in these expansions is extremely demanding. Here we employ an approximate expression for Eq. (2) that has been presented in full detail in [33]. In short the Hilbert space is divided in two regions: the interaction region and the asymptotic region. In the interaction region the potential energy is larger than the kinetic one whereas in the asymptotic region the kinetic energy is the dominating one. Approximate expressions for the wave function (2) are derived in both regions and matched smoothly at the reaction zone boundary. Using this model we calculated the cross-section for the electron-impact ionization of atomic hydrogen in its ground state. Fig. 2 shows the cross-section as function of the deflection angle of the positron and the secondary electron energy E_{e^-}. The positron impact energy is 500 eV and the electron is detected in the forward direction ($\hat{\boldsymbol{k}}_0 \| \hat{\boldsymbol{k}}_{e^-}$). Both the electron and the positron recede with equal velocities from the residual ion, i.e., $k_{e^-} = k_{e^+}$. The spectrum shown in Fig. 2 reveals a rich structure that can be associated with some of the terms in Eqs. (10)–(12). The peak at $\theta_{e^+} := \cos^{-1}(\hat{\boldsymbol{k}}_0 \cdot \hat{\boldsymbol{k}}_{e^+}) = \pi/2 \ \forall E_{e^-}$ is related to the

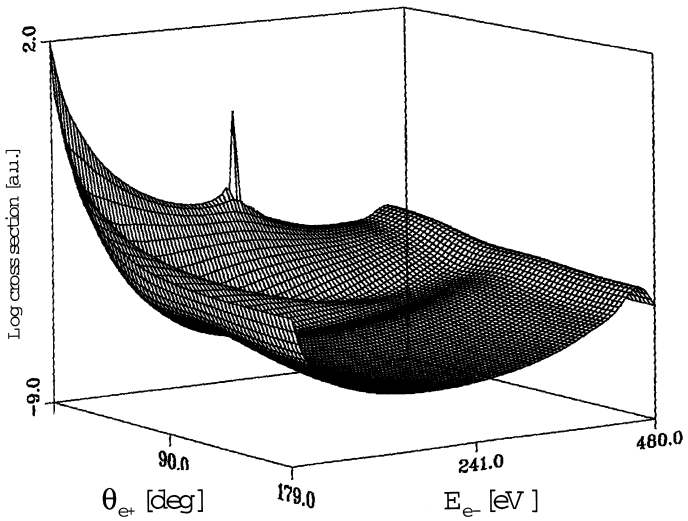

Fig. 2. The ionization cross-section of atomic hydrogen by positron impact as a function of the positron's scattering angle θ_{e^+} and the secondary electron energy E_{e^-}. The impact energy is 500 eV. The electron is detected in the forward direction along the direction of the incident positron. The positron energy in the final state is $E_{e^+} = (500 - E_{e^-} - 13.6)$ eV.

second term in Eq. (12), i.e., (cf. Fig. 1(d)), after scattering from the proton the positron can emerge into any direction since the proton is far more massive than the positron. Subsequently, the scattered positron collides with the electron that is then ionized. As the electron and the positron have equal masses they have to emerge perpendicular to each other and therefore the peak at $\theta_{e^+} = \pi/2$ (note that the electron is detected at the forward direction). The insets in Fig. 3(a) illustrate the evolution of this peak. The second peak starting at $E_{e^-} \approx 0, \theta_{e^+} \approx 0$ and extending to $E_{e^-} \approx 485$ eV, $\theta_{e^+} \approx \pi/2$ can be assigned to the fifth term in Eq. (12), i.e., (cf. Fig. 1(f)), after a positron–electron encounter the electron scatters off the proton. The monotonic shift of the position of this peak to higher deflection angles of the positron with increasing secondary electron energy is readily understood from the insets shown in Fig. 3(b). Eventually, this peak merges with the first one located at $\theta_{e^+} = \pi/2 \ \forall E_{e^-}$.

At $\theta_{e^+} = 0$, we notice three obvious structures: for $\theta_{e^+} = 0$ the cross-section is considerably large at $E_{e^-} \approx 0$. This is due to the nature of the Coulomb interaction that prefers soft collisions with minimal momentum transfer. In addition, the attractive electron–proton interaction implies a large density of states for electrons slowly moving in the proton frame of reference. This also increases the cross-section for soft electrons. At $E_{e^-} \approx 234$ eV the electron and the positron escape with nearly equal velocity and in the same direction. Thus, the electron moves in a low-lying continuum state of the positron. Since the electron–positron interaction is attractive the density of states available for the escaping electron is considerably increased when the electron approaches the positron and so does the cross-section [31,32]. At very high secondary electron energies, i.e., for complete energy loss of the positron the cross-section tends to drop (cf. Fig. 4 as well). This is due to a repulsion effect between the positron and the residual ion, i.e., to the vanishing density of states for the positron in the field of the positively charged proton. The exponential decrease of the cross-section is absent in the case of heavy ion impact since the ions hardy slow down by transferring, say 500 eV, energy to the secondary electron.

At lower incident energies the effects resulting from sequential binary collisions become smeared out as seen in Fig. 4 for an impact energy of 100 eV. This is because the momentum components present in the initial bound state become more important and the electron (to be ionized) cannot

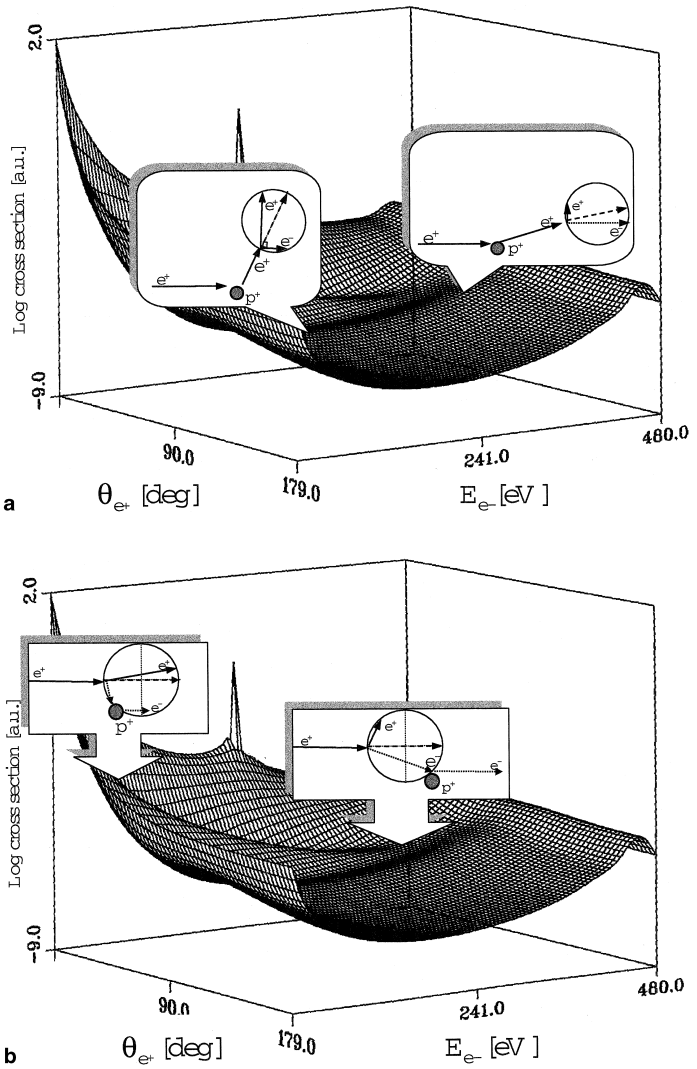

Fig. 3. (a) The same as in Fig. 2 with the scattering mechanisms leading to the peak at $\theta_{e^+} \approx \pi/2$ being sketched. (b) In this figure we illustrate schematically the reason for the evolution of the peak starting at $\theta_{e^+} \approx 0$ and $E_{e^-} \approx 0$ and extending to $\theta_{e^+} \approx \pi/2$ and $E_{e^+} \approx 0$.

be assumed to be at rest before the collisions. In contrast, the dynamical effects such as the structures discussed at $\theta_{e^+} = 0$ become more prominent.

3. Secondary electron ejection from surfaces by positron beams

In this section, we deal with the secondary electron emission from clean metallic surfaces following the impact of a positron beam. The utilization of positron beams for surface analysis has a long history of success [34–48]. Here we envisage a new technique in which a well-defined positron beam impinges on a metallic surface and ejects thereby secondary electrons. The emitted electron and the scattered positron are detected at the same time and their energies and emission directions are experimentally determined. The inset in Fig. 5 shows schematically the proposed

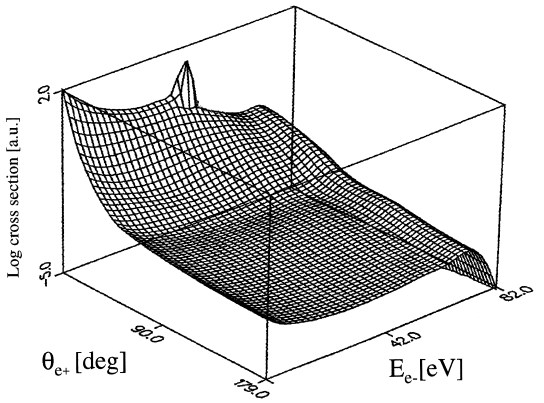

Fig. 4. The positron-impact ionization cross-section of hydrogen at the same geometrical arrangement as in Fig. 2, however, the incident energy is lowered to 100 eV.

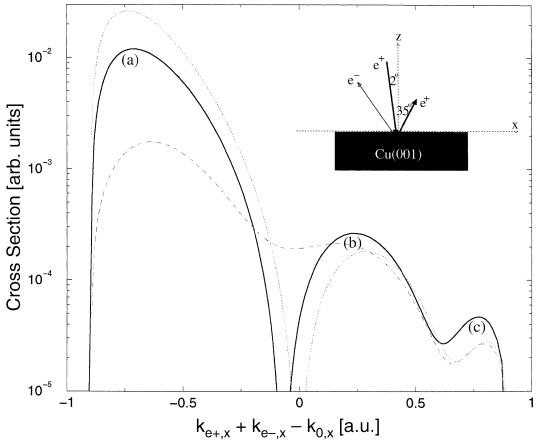

Fig. 5. The coincident probability rate for the emission of a positron and an electron with wave vectors $k_{e^+,x}$ and $k_{e^-,x}$ from a Cu(0 0 1) surface following the impact of a positron beam with wave vector $k_{0,x}$. As shown in the inset the electron and the positron are detected at equal positions (35°) with respect to the z-direction whereas the incident beam is tilted by 5° with respect to the z-axis. The incident energy is fixed at $E_0 = 65$ eV. The total excess energy of the escaping positron and electron is also fixed at $E_{\rm tot} = (k_{e^-}^2 + k_{e^+}^2)/2 = 60$ eV, i.e., the secondary electron is ejected from the vicinity of the Fermi level. The dotted curve is the result of the calculation for the same experimental set-up but the screening of the electron–positron interaction (i.e., η_1 in Eq. (A.5) is neglected all together ($\eta_1 = 0$)), whereas the dashed curve shows the results for a screening length of $\eta_1 = 1.2$ Å.

experiment. As will be shown below such measurements contain useful information on the one-particle spectral function of the occupied states.

If the electron–positron pair is emitted in a back-reflection mode (cf. inset of Fig. 5), we need to incorporate in a theoretical description the positron–lattice interaction [49,50] *and* the positron–electron correlation [51]. In this work we investigate first the electron–positron pair emission that is due to the electron–positron correlation only. Subsequently, we investigate the case where the crystal potential becomes involved.

3.1. Electron–positron correlation function

Let us assume that the system consisting of the solid and the positron beam is described by the Hamiltonian $H = H_s + H_{e^-e^+} + H_{e^+s}$. Here H_s is the Hamiltonian of the undisturbed surface. For simplicity we omit from our discussion the plasmon and the phonon fields. H_s describes then the electrons in the crystal static potential and is given by $H_s = \sum_{\boldsymbol{k},n,s} E_n(\boldsymbol{k}) a^\dagger_{\boldsymbol{k},n,s} a_{\boldsymbol{k},n,s}$, where $\boldsymbol{k}$ is the crystal momentum, $E_n(\boldsymbol{k})$ describes the electronic structure of the band with index n. The interaction of the positron with the crystal potential is given by H_{e^+s}. The electron creation and annihilation operators are given by $a^\dagger_{\boldsymbol{k},n,s}$ and $a_{\boldsymbol{k},n,s}$, respectively, and s is a spin index. Correlation and exchange effects between the electrons in the solid are assumed to be included in H_s in form of an effective one-particle potential, such the one derived within the density functional theory. The two-particle operator $H_{e^-e^+}$ induces the electron–positron pair emission and is expressed as

$$H_{e^-e^+} = \sum_{\alpha,\beta} \frac{-4\pi}{\Omega\epsilon} \frac{1}{|\boldsymbol{k}_0 - \boldsymbol{k}_{e^+}|^2 + q_s^2} \times a^\dagger_{\boldsymbol{k}_{e^-},\alpha} b^\dagger_{\boldsymbol{k}_{e^+},\beta} b_{\boldsymbol{k}_0,\beta} a_{\boldsymbol{q},\alpha} \delta(\boldsymbol{q} - (\boldsymbol{k}_{e^-} + \boldsymbol{k}_{e^+} - \boldsymbol{k}_0)), \tag{13}$$

where $b^\dagger$ and b are the positron creation and annihilation operators, α and β indicates the spin projections, Ω is the volume of the crystal, q_s is the screening wave vector of the electron–positron interaction which can be estimated, e.g. from the Thomas–Fermi model. The dielectric constant is ϵ.

The expression (13) accounts for interaction within the electron–positron pair and the electron–hole interaction in the final state.

At the time $t = 0$, long before the incoming positron hits the sample, the whole system is in the (initial) state $|i\rangle = b^{\dagger}_{\boldsymbol{k}_{e^+},\beta}|0\rangle$. After the collision, i.e., at $t \to \infty$, the final state $|f\rangle$ consists of an electron–positron pair and a hole state in the conduction band, more precisely $|f\rangle = a^{\dagger}_{\boldsymbol{k}_{e^-},\alpha} b^{\dagger}_{\boldsymbol{k}_{e^+},\beta} a_h|0\rangle$ (the operator a_h indicates the creation of the hole). The final state can be expanded in plane waves such that

$$|f\rangle = \frac{1}{\Omega^{1/2}} \sum_{\boldsymbol{k},\gamma} A^{*h}_{\gamma}(\boldsymbol{k}) a^{\dagger}_{\boldsymbol{k}_{e^-},\alpha} b^{\dagger}_{\boldsymbol{k}_{e^+},\beta} a_{\boldsymbol{k},\gamma}|0\rangle. \tag{14}$$

Here $A^{h}_{\gamma}(\boldsymbol{k})$ is the Fourier transform of the single-particle wave function of the conduction band electron with spin projection γ. According to the "golden rule" the transition probability rate is given by $\lim_{t\to\infty}(1/t)|T(t)|^2$, where

$$T(t) = \langle 0|a^{\dagger}_h b_{\boldsymbol{k}_{e^+},\beta} a_{\boldsymbol{k}_{e^-},\alpha} e^{-iHt} b^{\dagger}_{\boldsymbol{k}_{e^+},\beta}|0\rangle. \tag{15}$$

The expression (15) is nothing else but the electron–positron two-particle Green function $G^{(2)}_{e^-e^+}$ [52]. The cross-section (1) is obtained from $\lim_{t\to\infty}(1/t)|G^{(2)}_{e^-e^+}|^2$ after averaging over the quantum numbers not observed in the initial state and summing over those not resolved in the final state. Thus, the measurement of the electron-positron spectrum reveals the details of the two-particle Green function which in turn depends sensitively on the electron–positron correlation. In addition, as clear from Eqs. (14) and (15) the emission probability depends on $|A^{h}_{\gamma}(\boldsymbol{k})|^2$ which is the spectral function of the conduction band electrons (note that an integration of $|A^{h}_{\gamma}(\boldsymbol{k})|^2$ over $\boldsymbol{k}$ yields the energy-resolved density of states). These conclusions are valid only if the positron-induced electron emission takes place in response to an electron–positron correlation without an additional scattering of the electron–positron pair from the crystal potential. The latter case will be discussed in next section. The two-particle Green function can be expanded [52,53] to first-order in the electron–positron interaction to obtain numerically tractable expressions for the cross-section.

3.2. Electron–positron emission in reflection mode

As stated above the electron–positron pair emission induced by the interaction $H_{e^-e^+}$ can be related to the two-particle Green function which in turn can be expanded in terms of single-particle Green function that are numerically accessible, this transition amplitude is denoted hereafter by $T_{e^-e^+}$. However, in reflection mode emission, i.e., in situations as those shown in Fig. 5, it is clear from classical arguments that the crystal potential has to be involved. This is because a (classical) scattering of equal-mass particles cannot lead to a back-reflection of both of these particles. Therefore, we have to evaluate at least a second-order term in which the positron interacts both with the electron and the crystal. The total transition amplitude can thus be written as $\mathscr{T} = T_{e^-e^+} + T_{e^-e^+crys}$ where [54]

$$T_{e^-e^+crys} = \int\int d^3\boldsymbol{p}\; d^3\boldsymbol{q} \langle \boldsymbol{k}_{e^-}, \boldsymbol{k}_{e^+}|H_{e^-e^+} G^{(2)}_{e^-e^+}|\boldsymbol{p},\boldsymbol{q}\rangle \times \langle \boldsymbol{p}|W_{e^+crys}|\boldsymbol{k}_0\rangle \langle \boldsymbol{q}|\chi_{\epsilon(\boldsymbol{k})}\rangle. \tag{16}$$

In Eq. (16) $|\chi_{E(\boldsymbol{k})}\rangle$ is a single-particle occupied state of the electron before the ejection with $\boldsymbol{k}$ being the Bloch wave vector whereas $|\boldsymbol{q}\rangle \otimes |\boldsymbol{p}\rangle$ is a complete set of plane waves.

For the numerical calculations shown below we employ for the positron–crystal scattering potential $W_{e^-e^+crys}$ an approximate expression consisting of a non-overlapping muffin–tin ionic potentials V^{ion} ($W_{e^+crys} = \sum_i V^{ion}_i$). The form factor $\tilde{W}_{e^+crys} := \langle \boldsymbol{p}|W_{e^+crys}|\boldsymbol{k}_0\rangle$ can then be reduced to

$$\tilde{W}_{e^+crys} = \frac{N\sqrt{2\pi}f}{A_{uc}} \sum_{\ell} e^{-iK_z r_{\perp,\ell}} \sum_{\boldsymbol{g}_{\parallel}} \delta^{(2)}(\boldsymbol{g}_{\parallel} - \boldsymbol{K}_{\parallel}) \tilde{V}^{ion}(\boldsymbol{K}). \tag{17}$$

In Eq. (17), $\tilde{V}^{ion}(\boldsymbol{K})$ is the Fourier transform of V^{ion}, N is the number of ionic cores illuminated by the positron beam, A_{uc} is the volume of the two-dimensional unit cell, $\boldsymbol{g}_{\parallel}$ is the surface reciprocal lattice vector, ℓ enumerates the atomic layers with shortest distance $r_{\perp,\ell}$ with respect to the origin,

$\boldsymbol{K} = \boldsymbol{p} - \boldsymbol{k}_0$, and $f = \exp(\mathrm{i}\boldsymbol{p}\cdot\boldsymbol{r}_{\mathrm{e}^-})$ with $\boldsymbol{r}_{\mathrm{e}^-}$ referring to the position of the electron.

The electron–positron pair is interacting via $H_{\mathrm{e}^-\mathrm{e}^+}$. Thus, it is more appropriate to consider the electron–positron two-particle wave function. Due to the (two-dimensional) transitional symmetry of the crystal this two-particle wave function has to satisfy the Bloch theorem which imposes on the transition amplitude the following form:

$$T_{e^+\mathrm{crys}} \propto \sum_{\ell,\boldsymbol{g}_\parallel} \delta^{(2)}[\boldsymbol{g}_\parallel - (\boldsymbol{K}_\parallel - \boldsymbol{K}_{0,\parallel})] \times \mathscr{L}(\boldsymbol{g}_\parallel, \ell, \boldsymbol{K}, \boldsymbol{k}_{\mathrm{e}^-}, \boldsymbol{k}_{\mathrm{e}^+}, \boldsymbol{k}). \quad (18)$$

Here $\boldsymbol{K}_0 = \boldsymbol{k}_0 + \boldsymbol{k}$ and $\boldsymbol{K} = \boldsymbol{k}_{\mathrm{e}^+} + \boldsymbol{k}_{\mathrm{e}^-}$ are respectively the initial and the final wave vector of the electron–positron pair. The function $\mathscr{L}$ depends on the description of the momentum–space wave function $\langle \boldsymbol{q}|\chi_{\epsilon(\boldsymbol{k})}\rangle$ of the bound electron and the type of the expansion of the two-particle Green function. For a jellium-state momentum distribution and to a first-order expansion of the two-particle Green function in the interaction $H_{\mathrm{e}^-\mathrm{e}^+}$ the terms $T_{\mathrm{e}^+\mathrm{e}^-}$ and $T_{\mathrm{e}^-\mathrm{e}^+\mathrm{crys}}$ can be evaluated in closed form [54].

Eq. (18) has important implications:

1. The Bragg condition, expressed by the delta function in Eq. (18) implies that only the center-of-mass wave vector of the positron–electron pair is relevant for the diffraction process. This means that the electron–positron system as whole is diffracted when the parallel component of its wave vector is changed by $\boldsymbol{g}_\parallel$ during the collision. Note that in low energy electron or positron diffraction studies diffraction occurs when the change in the wave vector of the incident electron/positron matches $\boldsymbol{g}_\parallel$ [55,56]. The decisive difference to the electron–positron pair's diffraction is that a fixed $\boldsymbol{K}$ does not imply fixed $\boldsymbol{k}_{\mathrm{e}^+}$ and/or fixed $\boldsymbol{k}_{\mathrm{e}^-}$ since a momentum exchange within the positron–electron subsystem (mediated by $H_{\mathrm{e}^-\mathrm{e}^+}$) does not necessarily modify $\boldsymbol{K}$ (however, $\boldsymbol{k}_{\mathrm{e}^+} - \boldsymbol{k}_{\mathrm{e}^-}$ has then to change in a certain way to keep $\boldsymbol{K}$ fixed). Therefore, a definite change in $\boldsymbol{K}$ does not fix the amount of change in the positron's wave vector.
2. The *positions* of the electron–positron diffraction peaks are determined by the amount of change in $\boldsymbol{K}$, the function $\mathscr{L}$ that depends on $H_{\mathrm{e}^-\mathrm{e}^+}$, i.e., on the strength of the positron–electron correlation controls the *intensity* and *shape* of the individual diffraction peaks.
3. Usually, the wave vector $\boldsymbol{k}_\parallel$ of the initially bound Bloch electron is not resolved by the experiment. Thus, we have to average over it when calculating the cross-sections. This results in a smear-out effect of the diffraction pattern even in the case where $\boldsymbol{K}$ and $\boldsymbol{k}_0$ are experimentally sharply resolved. Note that such behavior does not occur in single positron or electron diffraction since in this case only the crystal potential is basically involved.
4. Experimentally, $\boldsymbol{K}_\parallel, \boldsymbol{g}_\parallel$ and $\boldsymbol{k}_{0,\parallel}$ can be measured with a sufficient accuracy. In such an experiment, the positions and widths of the diffraction peaks reflect the character of $\boldsymbol{k}_\parallel$, e.g., the maximal allowed width of the diffraction peak is k_{F}, where k_{F} is the Fermi wave vector.

Fig. 5 illustrates the above statements for a Cu(0 0 1) monocrystal. The positron incident energy is fixed at $E_0 = 65$ eV. The total excess energy of the escaping positron and electron is also fixed at $E_{\mathrm{tot}} = (k_{\mathrm{e}^-}^2 + k_{\mathrm{e}^+}^2)/2$ at 60 eV, i.e., the electron is ejected from the vicinity of the Fermi level. As clear from the inset in Fig. 5, $\boldsymbol{k}_0, \boldsymbol{k}_{\mathrm{e}^+}, \boldsymbol{k}_{\mathrm{e}^-}$ lie in the x–z plane, i.e., $\boldsymbol{K}_\parallel$ possesses only one non-vanishing component K_x along the x-axis. As indicated above, the component relevant to the positron–electron pair diffraction is in fact $K_x - k_{0,x}$. Therefore, we consider electron–positron emission probability rate as a function of $K_x - k_{0,x}$ (while E_{tot} and E_0 are fixed as stated above). The results shown in Fig. 5 are obtained after integration over $\boldsymbol{k}_\parallel$ (weighted with the density of states). In Fig. 5 we notice three prominent peaks labeled by (a), (b) and (c) which can be identified as diffraction peaks of the electron–positron pair. Since we integrated over the crystal momentum $\boldsymbol{k}_\parallel$ these peaks are broadened. Nonetheless, it is straightforward to show that the peak (a) can be associated with the $(-1, 0)$ diffracted beam whereas peak (b) corresponds to the specular diffraction of the electron–positron pair [the $(0, 0)$ beam] and finally the peak (c) can be assigned to the $(1, 0)$ diffracted beam. The heights of the three peaks are drastically different indicating that the electron–positron

scattering dynamics, as described by $\mathscr{L}$ in Eq. (18) has a strong influence on the spectrum in the range scanned in Fig. 5. In fact in some situations the diffraction might be removed altogether by the dynamical factor $\mathscr{L}$, i.e., if $\mathscr{L}$ vanishes in Eq. (18) the cross-section also vanish. We illustrate this behavior in Fig. 6, where a Fe(1 1 0) (BCC) monocrystal is used and the secondary electron is ejected deep from the conduction band. In this case the electron–positron spectrum becomes symmetric and sharply centered around the specular beam direction. In other words, the specular electron–positron beam in Fig. 5 (peak (b)) is shifted to the left and the beams (a) and (c) are completely suppressed.

In the final example, we concentrate on the differences and common features between the use of electron and positron beams for the secondary electron ejection. One obvious difference that is mentioned in the introduction is the presence of exchange effects when using electron beams. In Fig. 7(a) we analyze the spectrum of the escaping electron–electron pair following the impact of an electron beam. The feasibility of such experiments has already been demonstrated [57–60]. In Fig. 7(a) we notice two broad peaks at the wings of the spectrum. The asymmetry in the distribution is related the asymmetry in the experimental set-up as shown in the inset. Performing the same experiment with positron beams (Fig. 7(b)) the peak on the left survives almost unchanged while the one to the right diminishes. However, if we exchange the positions of the electron and the positron detectors as shown in Fig. 7(c) the peak to the right in Fig. 7(a) remains while that to the left disappears. Now combining Figs. 7(b) and (c) and

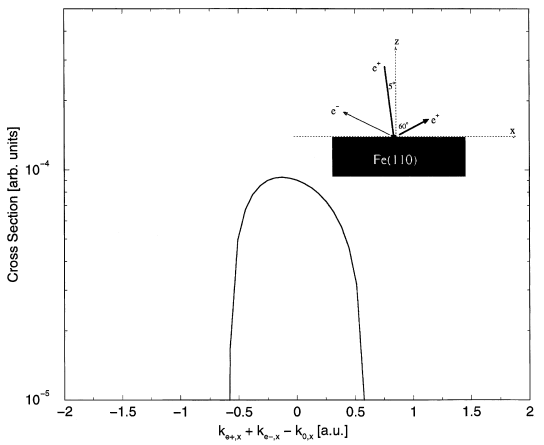

Fig. 6. The electron–positron emission from a Fe(1 1 0) (BCC) crystal. As shown in the inset the positron beam impinges at 5° with respect to the z-direction whereas the emitted electron and positron are detected at equal (60°) but opposite sides to the z-direction. The incident energy is 100 eV and the total energy of the escaping electron and positron is 90 eV.

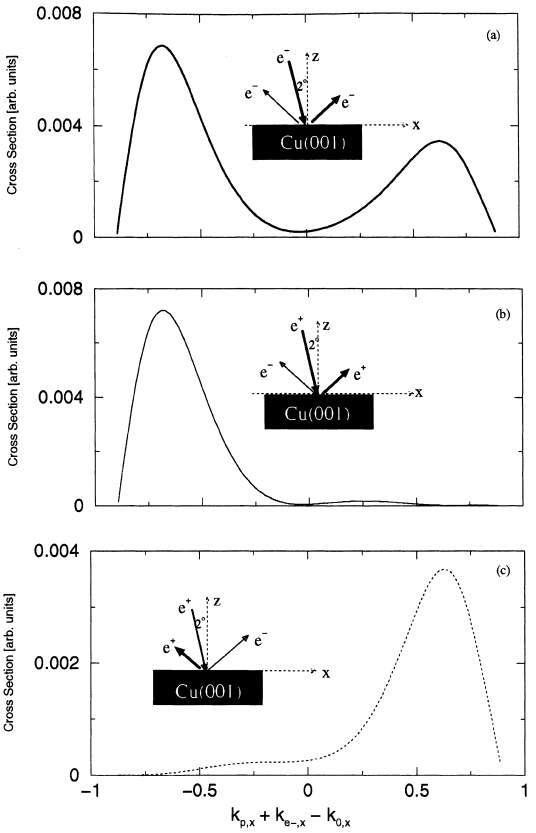

Fig. 7. (a) The simultaneous electron-pair emission from Cu(0 0 1) following the impact of 65 eV electron beam. The total energy of the electron pair is 60 eV. The angle of incidence of the electron beam with respect to the z-direction is 5° whereas the two emitted electrons emerge at opposite sides to the z-direction and under equal angles of 35° (cf. inset). (b) The same as (a) but we use positrons as a projectile instead of electrons (a). (c) The same as in (b) but the positron and the electron detectors are exchanged (cf. insets in (b) and (c)). The label $k_{p,x}$ in (c) indicates the wave vector of the scattered positron in case of positron impact or that of the electron when using electrons as projectiles.

the finding of Fig. 5 we can explain the origin of the structures in Fig. 7(a): the effect of exchange when using electron beams means basically that we cannot distinguish in which detector which electron is observed, i.e., roughly speaking, we have to consider the spectrum at a given arrangement of the detectors and the spectrum when the detectors are exchanged. In fact, Fig. 7(a) is readily obtained by combining Figs. 7(b) and (c). This means that in Fig. 7(a) one peak is due to the scattering dynamics of the pair from the crystal potential (the right wing peak) whereas the other peak is due to exchange. The origin of the large peak in Fig. 7(b) and, hence that in Fig. 7(a), lies in the diffraction of the emerging pair, as pointed out in the discussion of Fig. 5 (note that only the angle of incidence is changed from 5° in Fig. 5 to 2° in Fig. 7).

As a final remark we note that the above numerical calculations have been performed using the local screening of the electron–positron interaction with the screening length being estimated from the Thomas–Fermi theory. On the other hand it is well known that, in general, the screening has a non-local, frequency dependent character that is described by an appropriate dielectric function. The incorporation of such a non-local function in the present calculations leads to intractable numerical problems. One solution to this problem, that has been suggested recently [61], is to derive the screening length from the density of states at the Fermi level using full ab initio band-structure calculations. In the context of the present work we can get an insight into the effect of screening on the electron–positron spectra by varying the screening length within a reasonable range. For example, the calculation of Fig. 5 have been repeated with the screening being neglected altogether and with the screening being quite large (screening length is 1.2 Å). As clear from the Fig. 5, by varying the amount of screening the spectra are smeared out but the over-all structure is not destroyed.

4. Conclusions

In this work, we started by considering the mechanisms for electronic excitations of isolated atomic systems by low-energy positrons. Using a multiple-scattering expansion we analyzed the possible one- and multi-step scattering events and connected these to a classical analog. Dynamical effects due to the motion of the charged particles in a Coulomb field have also been discussed briefly. In the second part of this work we considered the electron–positron pair emission from metallic surfaces upon the impact of low-energy positron. Using a formal analysis we showed that the probability emission rate is connected to the two-particle Green operator of the interacting electron–positron pair. For emission in back-reflection mode we also included the effect of the crystal potential and pointed out that the diffraction of the electron–positron pair as an entity might take place leading to characteristic diffraction pattern. Finally, we discussed briefly the differences and common features when employing electron or positron electron beams to produce the secondary electrons.

Appendix A. Analytical evaluation of the scattering amplitude

In this section, we derive an analytical expression for the function $\mathscr{L}$ in Eq. (18). To this end we need assume simple, yet reasonable models for the electronic and crystal structure of the surface. The latter we describe with the aid of a muffin–tin form given by Eq. (17). For the description of the initial electronic distribution of the surface we resort to an effective one-particle theory and assume the initially bound electron to be described by the effective one-particle state vector $|\chi_k\rangle$. An expression for $|\chi_k\rangle$ can be derived by considering the ionic cores as a constant positive 'back-ground charge'. Within this *jellium model*, the resultant effective one-particle potential for the electron is a step potential V_0 at surface (as usual, $z = 0$ is located at the jellium edge). Within the metal volume V the conduction band electrons are treated as independent particles bound to the metal half space $z < 0$ by a potential barrier

$$V_0 = \epsilon_F + W, \tag{A.1}$$

where ϵ_F is the Fermi energy and W is the work function. The density of states is given by that of

the free-electron gas (apart from a factor 2 which accounts for the electronic spin states) $\rho_j = V/(4\pi^3)$. Thus the jellium wave function can be expressed in terms of reflection and transmission coefficients,

$$\langle \boldsymbol{r}_{e^-} | \chi_{\boldsymbol{k}} \rangle = \frac{1}{\sqrt{V}} \exp(\mathrm{i}\boldsymbol{k}_{\parallel} \cdot \boldsymbol{r}_{e^-,\parallel}) \times \begin{cases} \mathrm{e}^{\mathrm{i}k_z z_{e^-}} + R\mathrm{e}^{-\mathrm{i}k_z z_{e^-}}, & z < 0 \\ T\mathrm{e}^{-\gamma z_{e^-}}, & z > 0. \end{cases} \quad (A.2)$$

The reflection and transmission coefficients R and T are given by

$$R = \frac{k_z - \mathrm{i}\gamma}{k_z + \mathrm{i}\gamma}, \quad T = \frac{2k_z}{k_z + \mathrm{i}\gamma} \quad (A.3)$$

and $\gamma = \sqrt{2V_0 - k_z^2}$.

The final-state interaction of the vacuum charged particles with the metallic surface can be described by an image-charge potential. Asymptotically, this potential behaves as $-1/4z$. Thus, the final state (vacuum) wave function at a given asymptotic energy E_f can be approximated by

$$\phi_f(\boldsymbol{r}_{e^-}, \boldsymbol{r}_{e^+}) = (2\pi)^{-3} \exp[\mathrm{i}\boldsymbol{k}_{e^+} \cdot \boldsymbol{r}_{e^+} + \mathrm{i}\boldsymbol{k}_{e^-} \cdot \boldsymbol{r}_{e^-} - \mathrm{i}\varphi(\boldsymbol{r}_{e^-})]. \quad (A.4)$$

In Eq. (A.4) the term $\varphi(\boldsymbol{r}_{e^-}) = a\ln(2k_{e,z}z_{e^-})$ is the phase modification of the asymptotically free electron motion due to its image charge where $k_{e,z} = \hat{\boldsymbol{z}} \cdot \boldsymbol{k}_{e^-}$ and the Sommerfeld parameter, $a = -1/(4k_{e,z})$, indicates the strength of this interaction. In the case $a \equiv 0$ we end up with the final state being a product of two free-particle states. The final state energy is given by $E_f = k_{e^-}^2/2 + k_{e^+}^2/2$. The corresponding phase modification of the positron's motion due to the image change interaction can also be taken into account. However, in this case it has not been possible to obtain analytical results.

The electron–positron pair is coupled via the Coulomb screened potential

$$H_{e^-e^+} = \lim_{\eta_1 \to +0} \frac{-Z_{e^+} \exp(-\eta_1 |\boldsymbol{r}_{e^-} - \boldsymbol{r}_{e^+}|)}{|\boldsymbol{r}_{e^-} - \boldsymbol{r}_{e^+}|}, \quad (A.5)$$

where $Z_{e^+} = 1$ is the charge of the positron. A first rough estimate of the value of the cut-off factor, which quantifies the amount of screening of the electron–positron Coulomb interaction, derives from the Thomas–Fermi theory of screening. Here it is important to note that all the integrals shown below do exist in the limit of unscreened interaction ($\eta_1 \to 0$), as demonstrated explicitly below. Thus, we are able to test the influence of (local) screening effects by varying η_1.

By expanding the Green function to the first-order we can write the expression (16) as

$$F = -Z_{e^+} \lim_{\eta_1,\eta_2 \to +0} (2\pi)^{-3} \int \mathrm{d}^3\boldsymbol{q} \times \exp[\mathrm{i}(\boldsymbol{q} - \boldsymbol{k}_{e^+}) \cdot \boldsymbol{r}_{e^-}] \tilde{H}_{e^-e^+}(\boldsymbol{k}_{e^+} - \boldsymbol{q}, \eta_1) \times \frac{1}{\boldsymbol{K}_-^2 - \boldsymbol{q}^2 - \mathrm{i}\eta_2} \tilde{W}_{e^+\,\mathrm{crys}}(\boldsymbol{q} - \boldsymbol{k}_0), \quad (A.6)$$

where $\boldsymbol{K}_- := \boldsymbol{k}_{e^-} - \boldsymbol{k}_{e^+}$. Upon substituting the form factor $\tilde{W}_{e^+\,\mathrm{crys}}(\boldsymbol{q} - \boldsymbol{k}_0)$ (Eq. (17)) into Eq. (A.6) we obtain

$$F = \frac{-2(2\pi)^{-3/2} Z_{e^+} N}{A_{\mathrm{uc}}} \times \lim_{\eta_1,\eta_2 \to +0} \sum_{\ell,\boldsymbol{g}_{\parallel}} \int \mathrm{d}^3\boldsymbol{q}\ \delta^{(2)}(\boldsymbol{g}_{\parallel} - \boldsymbol{K}_{\parallel}) \times \exp[\mathrm{i}(\boldsymbol{q} - \boldsymbol{k}_{e^+}) \cdot \boldsymbol{r}_{e^-}] \times \frac{\exp(-\mathrm{i}K_z r_{\perp,\ell}) \tilde{V}^{\mathrm{ion}}(\boldsymbol{K})}{(|\boldsymbol{k}_{e^+} - \boldsymbol{q}|^2 + \eta_1^2)(\boldsymbol{K}_-^2 - \boldsymbol{q}^2 - \mathrm{i}\eta_2)}. \quad (A.7)$$

Changing variables from $\boldsymbol{q}$ to $\boldsymbol{K}$ the expression (16) for $T_{e^-e^+\mathrm{crys}}$ simplifies to

$$T_{e^-e^+\mathrm{crys}} = \int \mathrm{d}^3\boldsymbol{K}\ \mathscr{F}(\boldsymbol{K}) I(\boldsymbol{K}), \quad (A.8)$$

where

$$\mathscr{F} := \frac{-2(2\pi)^{-3/2} Z_{e^+} N}{A_{\mathrm{uc}}} \lim_{\eta_1,\eta_2 \to +0} \sum_{\ell,\boldsymbol{g}_{\parallel}} \delta^{(2)}(\boldsymbol{g}_{\parallel} - \boldsymbol{K}_{\parallel}) \times \frac{\exp(-\mathrm{i}K_z r_{\perp,\ell}) \tilde{V}^{\mathrm{ion}}(\boldsymbol{K})}{(|\boldsymbol{Q} - \boldsymbol{K}|^2 + \eta_1^2)[\boldsymbol{K}_-^2 - (\boldsymbol{K} + \boldsymbol{k}_0)^2 - \mathrm{i}\eta_2]}. \quad (A.9)$$

In Eq. (A.9) the momentum transfer vector $\boldsymbol{Q} := \boldsymbol{k}_{e^+} - \boldsymbol{k}_0$ has been defined. Using Eq. (A.4) for the final-state, the function $I(\boldsymbol{K})$ which occurs in Eq. (A.8) is readily deduced to be

$$I(\boldsymbol{K}) = (2\pi)^{-3/2} \int \mathrm{d}^3\boldsymbol{r}_{\mathrm{e}^-}\ \exp[-\mathrm{i}(\boldsymbol{Q} + \boldsymbol{k}_{\mathrm{e}^-} - \boldsymbol{K}) \cdot \boldsymbol{r}_{\mathrm{e}^-} + \mathrm{i}\varphi(\boldsymbol{r}_{\mathrm{e}^-})]\chi_{\boldsymbol{k}}(\boldsymbol{r}_{\mathrm{e}^-}). \tag{A.10}$$

Using the integral representation

$$z^{-a} = \frac{1}{\Gamma(a)} \int_0^\infty \mathrm{d}t\ \exp(-zt)t^{a-1}, \quad \Re(a) > 0,\ \ \Re(z) > 0, \tag{A.11}$$

the logarithmic phase in the integral (A.10) can be rewritten as

$$\exp(\mathrm{i}\varphi) = \lim_{\eta_3 \to +0} \frac{1}{\Gamma(\alpha)} \int_0^\infty \mathrm{d}t\, \exp(-\xi \cdot \boldsymbol{r}_{\mathrm{e}^-})\, t^{\alpha-1}, \tag{A.12}$$

where $\alpha = -\mathrm{i}a + \eta_3$ (we recall $a = -1/(4k_{e,z})$) and $\boldsymbol{\xi} := 2k_{e,z}t\hat{\boldsymbol{z}}$. Thus the integral $I(\boldsymbol{K})$ evaluates to

$$I(\boldsymbol{K}) = \lim_{\eta_3 \to +0} \frac{1}{\Gamma(\alpha)} \int_0^\infty \mathrm{d}t\, t^{\alpha-1} \tilde{\chi}_{\boldsymbol{k}}(\boldsymbol{\Lambda}, t), \tag{A.13}$$

where

$$\tilde{\chi}_{\boldsymbol{k}}(\boldsymbol{\Lambda}, t) = \mathrm{i}\sqrt{\frac{2\pi}{V}}\delta^{(2)}(\boldsymbol{k}_\parallel - \boldsymbol{\Lambda}_\parallel) \times \left(\frac{1}{\Lambda_z - k_z} + \frac{R}{\Lambda_z + k_z} - \frac{T}{\Lambda_z - \mathrm{i}\gamma}\right). \tag{A.14}$$

The vector $\boldsymbol{\Lambda}$ is given by $\boldsymbol{\Lambda} := \boldsymbol{Q} - \boldsymbol{K} + \boldsymbol{k}_{\mathrm{e}^-} - \mathrm{i}\boldsymbol{\xi}$. For V^{ion} we employ the screened Coulomb potential

$$V^{\mathrm{ion}}(\boldsymbol{r}_{\mathrm{p}}) = Z_{\mathrm{eff}}/r_{\mathrm{e}^+} \exp(-\lambda_{\mathrm{eff}} r_{\mathrm{e}^+}). \tag{A.15}$$

The effective parameters $Z_{\mathrm{eff}}, \lambda_{\mathrm{eff}}$ account for the screening of pure ionic field due to the presence of the localized positive cores and the delocalized electrons. Thus, Eq. (A.8) can be reduced to

$$T_{\mathrm{e}^-\mathrm{e}^+\mathrm{crys}} = \lim_{\eta_1,\eta_2,\eta_3 \to +0} \frac{-NZ_{\mathrm{e}^+}Z_{\mathrm{eff}}}{\pi^2 A_{\mathrm{uc}}\Gamma(\alpha)} \times \int_0^\infty \mathrm{d}t\, t^{\alpha-1} \sum_{\ell,\boldsymbol{g}_\parallel} II(t, \ell, \boldsymbol{g}_\parallel), \tag{A.16}$$

where

$$II(t, \ell, \boldsymbol{g}_\parallel) := \int_{-\infty}^{\infty} \mathrm{d}K_z\, Y(K_z, t, \ell, \boldsymbol{g}_\parallel) \tag{A.17}$$

and

$$Y(K_z, t, \ell, \boldsymbol{g}_\parallel) = \exp(-\mathrm{i}K_z r_{\perp,\ell})\tilde{\chi}_{\boldsymbol{k}}(\boldsymbol{\Lambda}, \boldsymbol{K}_\parallel = \boldsymbol{g}_\parallel) \times \left[|\boldsymbol{Q}_\parallel - \boldsymbol{g}_\parallel|^2 + (Q_z - K_z)^2 + \eta_1^2\right]^{-1} \times \left[\boldsymbol{K}_-^2 - |\boldsymbol{k}_{0,\parallel} + \boldsymbol{g}_\parallel|^2 - (k_{i,z} + K_z)^2 - \mathrm{i}\eta_2\right]^{-1} \times \left[\boldsymbol{g}_\parallel^2 + K_z^2 + \lambda_{\mathrm{eff}}^2\right]^{-1}. \tag{A.18}$$

An expression for the integral (A.17) is obtained by converting K_z to a complex variable and considering the improper contour integral

$$II(t, \ell, \boldsymbol{g}_\parallel) = \lim_{\rho \to \infty} \oint_{\partial G_\rho} \mathrm{d}K_z\, Y(K_z, t, \ell, \boldsymbol{g}_\parallel) \tag{A.19}$$

since $r_{\perp,\ell} < 0$, $(r_{\perp,\ell} = -d_z/2)$ we choose the domain G as the upper half of the complex plane, i.e., $G = \{K_z |\ \Im(K_z) > 0, |K_z| < \rho\}$. The function $Y(K_z)$ is meromorphic is G, i.e., it only possesses isolated singularities and can thus be evaluated via calculus of residues. The poles of $Y(K_z)$ in G depend on the sign of $k_{e,z}$ and hence on the geometry in which the experiment is performed. In a transmission experiment $k_{e,z}$ is negative whereas $k_{e,z} > 0$ in reflection geometry. Here we perform the calculations in reflection geometry, similar considerations apply to transmission mode. The poles of $Y(K_z)$ in G are determined as

$$z_0 = Q_z + \mathrm{i}\left[|\boldsymbol{Q}_\parallel - \boldsymbol{g}_\parallel|^2 + \eta_1^2\right]^{1/2}, \tag{A.20}$$

$$z_1 = \begin{cases} -k_{i,z} - \left[\boldsymbol{K}_-^2 - |\boldsymbol{k}_{0,\parallel} + \boldsymbol{g}_\parallel|^2 - \mathrm{i}\eta_2\right]^{1/2}, \\ \quad \text{if} \quad \boldsymbol{K}_-^2 > |\boldsymbol{k}_{0,\parallel} + \boldsymbol{g}_\parallel|^2, \\ -k_{i,z} + \left[\boldsymbol{K}_-^2 - |\boldsymbol{k}_{0,\parallel} + \boldsymbol{g}_\parallel|^2 - \mathrm{i}\eta_2\right]^{1/2}, \\ \quad \text{if} \quad \boldsymbol{K}_-^2 < |\boldsymbol{k}_{0,\parallel} + \boldsymbol{g}_\parallel|^2, \end{cases} \tag{A.21}$$

$$z_2 = \mathrm{i}(\boldsymbol{g}_\parallel^2 + \lambda_{\mathrm{eff}}^2)^{1/2}. \tag{A.22}$$

Thus, the integral (A.19) can be expressed as

$$II(t,\ell,\boldsymbol{g}_\parallel)=2\pi\mathrm{i}\sum_{v=0}^{2}Res_{z_v}Y(K_z,t,\ell,\boldsymbol{g}_\parallel). \tag{A.23}$$

Inserting Eq. (A.23) into Eq. (A.8) the remaining t integral can be carried out analytically by using the integral representation of the β function,

$$\int_0^\infty t^{\mu-1}(1+\beta t)^{-\nu}\,\mathrm{d}t=\beta^{-\mu}B(\mu,\nu-\mu),$$
$$|\arg\beta|<\pi,\ \ \Re(\nu)>\Re(\mu)>0. \tag{A.24}$$

Furthermore, using the relation $B(x,y)=\Gamma(x)\Gamma(y)/\Gamma(x+y)$ we end up with the expression

$$T_{\mathrm{e^-e^+crys}}=\sqrt{\frac{8}{\pi V}}\frac{Z_{\mathrm{e^+}}Z_{\mathrm{eff}}N}{A_{\mathrm{uc}}}\mathrm{e}^{-2\pi a/3}\Gamma(1+\mathrm{i}a)$$
$$\times\exp(\mathrm{i}a\ln 2k_{e,z})\sum_{\ell,\boldsymbol{g}_\parallel}\delta^{(2)}(\boldsymbol{k}_\parallel-\boldsymbol{Q}_\parallel+\boldsymbol{g}_\parallel-\boldsymbol{k}_{e,\parallel})$$
$$\times(\mathscr{L}_0+\mathscr{L}_1+\mathscr{L}_2), \tag{A.25}$$

from which we obtain the desired formula for the function $\mathscr{L}$ in Eq. (18):

$$\mathscr{L}=\sqrt{\frac{8}{\pi V}}\frac{Z_{\mathrm{e^+}}Z_{\mathrm{eff}}N}{A_{\mathrm{uc}}}\mathrm{e}^{-2\pi a/3}\Gamma(1+\mathrm{i}a)$$
$$\times\exp(\mathrm{i}a\ln 2k_{e,z})(\mathscr{L}_0+\mathscr{L}_1+\mathscr{L}_2). \tag{A.26}$$

The functions $\mathscr{L}_0$, $\mathscr{L}_1$ and $\mathscr{L}_2$ are given by

$$\mathscr{L}_0=\exp(-\mathrm{i}z_0r_{\perp,\ell})\mathscr{B}_0\left[2\mathrm{i}|\boldsymbol{Q}_\parallel-\boldsymbol{g}_\parallel|\right]^{-1}$$
$$\times\left[\boldsymbol{K}_-^2-|\boldsymbol{k}_{0,\parallel}+\boldsymbol{g}_\parallel|^2-(k_{i,z}+z_0)^2\right]^{-1}$$
$$\times\left[\boldsymbol{g}_\parallel^2+z_0^2+\lambda_{\mathrm{eff}}^2\right]^{-1}. \tag{A.27}$$

In case $\boldsymbol{K}_-^2>|\boldsymbol{k}_{0,\parallel}+\boldsymbol{g}_\parallel|^2$ we obtain for $\mathscr{L}_1$

$$\mathscr{L}_1=\frac{-1}{2}\exp(-\mathrm{i}z_1r_{\perp,\ell})\mathscr{B}_1$$
$$\times\left[|\boldsymbol{Q}_\parallel-\boldsymbol{g}_\parallel|^2+(Q_z-z_1)^2\right]^{-1}$$
$$\times\left[\boldsymbol{K}_-^2-|\boldsymbol{k}_{0,\parallel}+\boldsymbol{g}_\parallel|^2\right]^{-1/2}\left[\boldsymbol{g}_\parallel^2+z_1^2+\lambda_{\mathrm{eff}}^2\right]^{-1}, \tag{A.28}$$

whereas if $\boldsymbol{K}_-^2<|\boldsymbol{k}_{0,\parallel}+\boldsymbol{g}_\parallel|^2$ the following relation is valid:

$$\mathscr{L}_1=\frac{-\mathrm{i}}{2}\exp(-\mathrm{i}z_1r_{\perp,\ell})\mathscr{B}_1$$
$$\times\left[|\boldsymbol{Q}_\parallel-\boldsymbol{g}_\parallel|^2+(Q_z-z_1)^2\right]^{-1}$$
$$\times\left[-\boldsymbol{K}_-^2+|\boldsymbol{k}_{0,\parallel}+\boldsymbol{g}_\parallel|^2\right]^{-1/2}$$
$$\times\left[\boldsymbol{g}_\parallel^2+z_1^2+\lambda_{\mathrm{eff}}^2\right]^{-1}. \tag{A.29}$$

Finally, the expression for $\mathscr{L}_2$ reads

$$\mathscr{L}_2=\frac{-\mathrm{i}}{2\sqrt{\boldsymbol{g}_\parallel^2+\lambda_{\mathrm{eff}}^2}}\exp(-\mathrm{i}z_2r_{\perp,\ell})\mathscr{B}_2$$
$$\times\left[|\boldsymbol{Q}_\parallel-\boldsymbol{g}_\parallel|^2+(Q_z-z_2)^2\right]^{-1}$$
$$\times\left[\boldsymbol{K}_-^2-|\boldsymbol{k}_{0,\parallel}+\boldsymbol{g}_\parallel|^2-(k_{i,z}+z_2)^2\right]^{-1}. \tag{A.30}$$

The functions $\mathscr{B}_j$, $j=0,1,2$, have been defined as

$$\mathscr{B}_j:=(b_j-k_z)^{-\mathrm{i}a-1}+R(b_j+k_z)^{-\mathrm{i}a-1}$$
$$-T(b_j-\mathrm{i}\gamma)^{-\mathrm{i}a-1}, \tag{A.31}$$

where $b_j:=\boldsymbol{Q}_z-z_j+k_{e,z}$.

References

[1] C.D. Lin, Phys. Rep. 257 (1) (1995) 1.
[2] L.H. Thomas, Proc. Roy. Soc. A 114 (1927) 561.
[3] K. Dettmann, G. Leibfried, Z. Phys. D 218 (1969) 1.
[4] R. Shakschaft, J.M. Wadehra, Phys. Rev. A 22 (1980) 968.
[5] R. Shakeshaft, L. Spruch, Phys. Rev. Lett. 41 (1978) 1037.
[6] R. Shakeshaft, L. Spruch, J. Phys. B 11 (1978) L457.
[7] J.S. Briggs, J. Phys. B 19 (1986) 703.
[8] J.S. Briggs, Comments At. Mol. Phys. 23 (1989) 155.
[9] M. Brauner, J.S. Briggs, J. Phys. B 24 (1991) 2227.
[10] J. Berakdar, H. Klar, J. Phys. B 26 (1993) 3891.
[11] A. Salin, J. Phys. B 2 (1969) 631.
[12] J.H. Macek, Phys. Rev. A 1 (1970) 235.
[13] Y.B. Band, J. Phys. B 18 (1974) 2557.
[14] K. Dettmann, K.G. Harrison, M.W. Lucas, J. Phys. B 7 (1974) 269.
[15] M.M. Duncan, M.G. Menendez, F.L. Eisele, J.H. Macek, Phys. Rev. A 15 (1977) 1785.
[16] M. Suter, C.R. Vane, I.A. Sellin, S.B. Elston, G.D. Alton, R.S. Thoe, R. Lauber, Phys. Rev. Lett. 41 (1978) 399.
[17] G.A. Glas, P. Engar, S.D. Berry, M. Breining, R. Deserio, S.B. Elston, I.A. Sellin, Nucl. Instr. and Meth. B 10/11 (1985) 138.

[18] C.R. Vane, I.A. Sellin, M. Suter, G.D. Alton, S.B. Elston, P.M. Griffin, R.S. Thoe, Phys. Rev. Lett. 40 (1978) 1020.
[19] G. Bissinger, J.M. Joyce, R. Mehta, Nucl. Instr. and Meth. B 40/41 (1989) 33.
[20] J.O.P. Pederson, P. Hvelplund, A.G. Petersen, P.D. Fainstein, J. Phys. B 24 (1991) 4001.
[21] D.H. Lee, P. Richard, T.J.M. Zouros, J.M. Sanders, J.L. Shinpangh, H. Hidmi, Phys. Rev. A 24 (1990) 97.
[22] J. Berakdar, J.S. Briggs, H. Klar, Z. Phys. D 24 (1992) 351.
[23] M. Brauner, J.S. Briggs, J. Phys. B 19 (1986) L325.
[24] A. Kövér, R.M. Finch, G. Laricchia, M. Charlton, J. Phys. B 30 (1997) L507.
[25] A. Kövér, G. Laricchia, M. Charlton, J. Phys. B 27 (1994) 2409.
[26] A. Kövér, G. Laricchia, M. Charlton, J. Phys. B 25 (1992) L613.
[27] D.R. Schultz, R.E. Olson, C.O. Reinhold, J. Phys. B 24 (1990) 521.
[28] D.R. Schultz, C.O. Reinhold, J. Phys. B 23 (1990) L9.
[29] Mandal, K. Roy, N.C. Sil, Phys. Rev. A 33 (1986) 756.
[30] R.A. Sparrow, R.E. Olson, J. Phys. B 27 (1994) 2647.
[31] A. Kövér, G. Laricchia, Phys. Rev. Lett. 80 (1998) 5309.
[32] J. Berakdar, Phys. Rev. Lett. 81 (1998) 1393.
[33] J. Berakdar, Phys. Rev. Lett. 78 (1997) 2712.
[34] H. Kuzmany, Solid-State Spectroscopy. An Introduction, Springer, Berlin, 1998.
[35] R. Krause-Rehberg, H.S. Leipner, Positron Annihilation in Semiconductors. Defect Studies, Springer, Berlin, 1999.
[36] R Suzuki, G. Amarendra, T. Ohdaira, T. Mikado, Appl. Surf. Sci. 149 (1–4) (1999) 66–70.
[37] T. Ohdaira, R. Suzuki, T. Mikado, Surf. Sci. 433–435 (1999) 239.
[38] T. Ohdaira, R. Suzuki, T. Mikado, T. Yamazaki, Mater. Sci. Forum 255–257 (1997) 769.
[39] T.E.M. Staab, R. Krause-Rehberg, B. Kieback, J. Mater. Sci. 34 (1999) 3833.
[40] N. Bouarissa, M. Certier, N. Amrane, H. Aourag, Mater. Sci. Engrg. B 54 (1998) 161.
[41] R. Suzuki, T. Ohdaira, A. Uedono, S. Ishibashi, A. Matsuda, S. Yoshida, Y. Ishida, S. Niki, P.J. Fons, T. Mikado, T. Yamazaki, S. Tanigawa, Y.K. Cho, Mater. Sci. Forum 255–257 (1997) 714.
[42] R. Zhang, H. Cao, J.-P. Yuan, C.-M. Huang, Q. Zhang, T.C. Sandreczki, B. Nielsen, P. Asoka-Kumar, R. Suzuki, T. Ohdaira, Y.C. Jean, Mater. Sci. Forum 255–257 (1997) 704.
[43] N. Bouarissa, A.B. Walker, H. Aourag, J. Appl. Phys. 83 (1998) 3643.
[44] E. Jung, H.Q. Zhou, S. Starnes, R. Venkataraman, A.H. Weiss, Appl. Surf. Sci. 116 (1997) 318.
[45] A. Goodyear, A.P. Knights, P.G. Coleman, Phys. Lett. A 212 (1996) 221.
[46] P. Hautojarvi, C. Corbel, Positron Spectroscopy of Solids, School of Physics 'Enrico Fermi', Course CXXV, IOS Press, Amsterdam, Netherlands, 1995, p. 491.
[47] A. Kawasuso, S. Okada, Phys. Rev. Lett. 81 (1998) 2659.
[48] Y. Nagashima, Y. Morinaka, T. Kurihara, Y. Nagai, T. Hyodo, T. Shidara, K. Nakahara, Phys. Rev. B 58 (1998) 12676.
[49] A. Weiss, E. Jung, J.H. Kim, A. Nangia, R. Venkataraman, S. Starnes, G. Brauer, Appl. Surf. Sci. 116 (1997) 311.
[50] C.B. Duke, A. Paton, A. Lazarides, D. Vasumathi, K.F. Canter, Phys. Rev. B 55 (1997) 7181.
[51] A. Rubaszek, in: Proceedings of the International School of Physics 'Enrico Fermi', Course CXXV, Positron Spectroscopy of Solids, IOS Press, Amsterdam, Netherlands, 1995, p. 285.
[52] A.A. Abrikosov, L.P. Gorkov, I.E. Dzyaloshinski, Methods of Quantum Field Theory in Statistical Physics, Dover, New York, 1975.
[53] N. Fominykh, J. Henk, J. Berakdar, P. Bruno, H. Gollisch, R. Feder, Solid State Commun. 113 (2000) 665.
[54] J. Berakdar, Unpublished.
[55] J.B. Pendry, Low Energy Electron Diffraction, Academic Press, London, 1974.
[56] M.A. van Hove, W.H. Weinberg, C.-M. Chan, Low Energy Electron Diffraction, Springer Series in Surface Science, Springer, Berlin, 1986.
[57] I.E. McCarthy, E. Weigold, Rep. Prog. Phys. 54 (1991) 789.
[58] M. Vos, I.E. McCarthy, Rev. Mod. Phys. 67 (1995) 713.
[59] A.S. Kheifets, S. Iacobucci, A. Ruoccoa, R. Camilloni, G. Stefani, Phys. Rev. B 57 (1998) 7380.
[60] J. Kirschner, O.M. Artamonov, S.N. Samarin, Phys. Rev. Lett. 75 (1995) 2424.
[61] J. Berakdar, H. Gollisch, R. Feder, Solid State Commun. 112 (10) (1999) 587.